# Nanotechnology, Nanomaterials

# Synthesize Silver Nanoprisms by a Thermal Growth Method

Y. Yang, M. Klug, Q. Hu, D. Jin, N. Fang

Sponsorship: National Science Foundation, Air Force Office of Scientific Research

Silver nanoprisms are plasmonic nanostructures that have attracted much attention because of their strong shape-dependent optical properties and related applications, e.g., surface-enhanced Raman scattering, near-field optical probes, and contrast agents for biomedical imaging. The chemically synthesized silver nanoplates have an extraordinary anisotropy due to the large ratio of lateral dimension to thickness. They support low-loss localized surface plasmon resonance and extremely high electromagnetic-field enhancement. Recently several methods have been developed to synthesize the silver triangular nanoprisms, such as NaBH4 reduction, light-mediated growth, thermal growth.

Here we synthesize silver nanoprisms via a thermal growth method and investigate the dependence of the nanoprisms' size, shape, and concentration on the chemical reaction conditions. We first change the reaction time. As shown in Figure 1(a) and (b), for longer reaction times the size of nanoprisms is larger, but the concentration is smaller. Most nanoprisms are triangles. In Figure 1(c) and (d), the poly (vinyl pyrrolidone) (PVP) solution is condensed by 2 times and 4 times, respectively, compared to the original value mentioned in Washio et al. We find the size and concentration have no obvious changes. It is interesting that when we dilute the PVP solution, shapes other than triangles appear. For example, the triangles with missing corners (Figure 2(a)), the hexagons (Figure 2(b)), and the triangles with huge size (Figure 2(c)). The thermally grown silver nanoprisms have good crystalline structure, which is demonstrated by X-ray diffraction (XRD) measurement (Figure 2(d)). Therefore, we have grasped a definitive procedure for the synthesis of silver nanoprisms based on the thermal growth method. The nucleation and growth of triangular prisms are kinetically controlled by the reduction rate and PVP concentration. These results are valuable for the study of nanoparticle-based photonic and plasmonic devices.

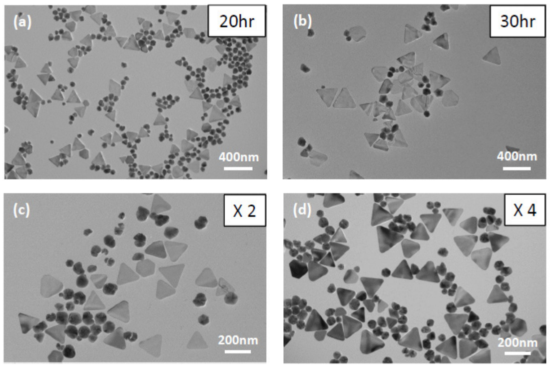

▲Figure 1: TEM images of thermally synthesized silver nanoprisms with different reaction times (a) 20hr and (b) 30hr and condensed PVP solutions whose concentrations are (c) 2- and (d) 4-times more than original solution.

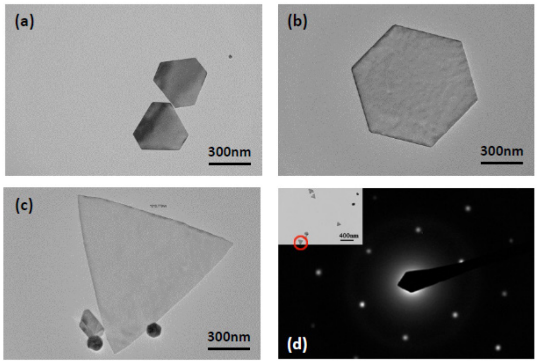

▲Figure 2: (a)-(c)TEM images of thermally synthesized silver nanoprisms with different facial shapes. (d) Detected XRD pattern shows crystalline structure in the silver nanoprisms.

## FURTHER READING

- Q. Zhang, N. Li, J, Goeb, Z. Lu, and Y. Yin, "A Systematic Study of the Synthesis of Silver Nanoplates: Is Citrate a "Magic" Reagent?," *J. Am. Chem. Soc.*, vol. 133, pp. 18931–18939, 2011.
- R. Jin, Y. C. Cao, E. Hao, G. S. Métraux, G. C. Schatz, and C. A. Mirkin, "Controlling anisotropic nanoparticle growth through plasmon excitation," *Nature*, vol. 425, pp. 487-490, 2003.
- I. Washio, Y. Xiong, Y. Yin, and Y. Xia, "Reduction by the End Groups of Poly(vinyl pyrrolidone): A New and Versatile Route to the Kinetically Controlled Synthesis of Ag Triangular Nanoplates," *Adv. Mater.* vol. 18, pp. 1745, 2006.

# Large-Area Self-Assembly of Lead Sulfide Nanocrystals

M. Weidman, R. Hoffman, W. Tisdale

Sponsorship: Department of Energy, National Science Foundation GRFP

Lead sulfide (PbS) nanocrystals, or quantum dots (QDs), are a useful material because their band gap is dependent on their physical size. By synthesizing the QDs to have diameters in the range of 4-8 nm, we are able to tune their light absorption and emission over a wavelength range of 1000-1800 nm. This tunability makes PbS QDs attractive for applications such as photovoltaics, photodetection, and near-infrared light emission. In most of these applications, the colloidal QDs are deposited as a thin film for their end use. In these thin films, it is desirable to have the QDs assembled in a well-ordered arrangement so as to (1) maximize the amount of QDs in a given volume and (2) maximize the rate at which charge carriers can move throughout the film.

Through synthesis of QD ensembles with low size dispersity (size distribution standard deviation < 3% mean size), we have observed large-area self-assembly of these nanocrystals into highly ordered superlattice structures. These superlattices can be formed through simple laboratory methods such as drop-casting or spin-coating. Figure 1a presents a transmission electron micrograph of a QD superlattice that is approximately 6 layers thick into the plane of the image. We have prepared large-area films by drop-casting concentrated suspensions of the QDs onto silicon wafers, resulting in a 1x1 cm film. The grazing-incidence small-angle X-ray scattering pattern from such a film is shown in Figure 1b. The discrete, high intensity pattern indicates the formation of a single crystal superlattice that indexes to that of a body-centered cubic structure. We present the wide-angle X-ray scattering pattern of the same sample in Figure 1c, which shows that the atomic planes of the individual nanocrystals are aligned in the film as well. This degree of ordering ensures a high packing density for the QDs and could lead to interesting transport properties within the film.

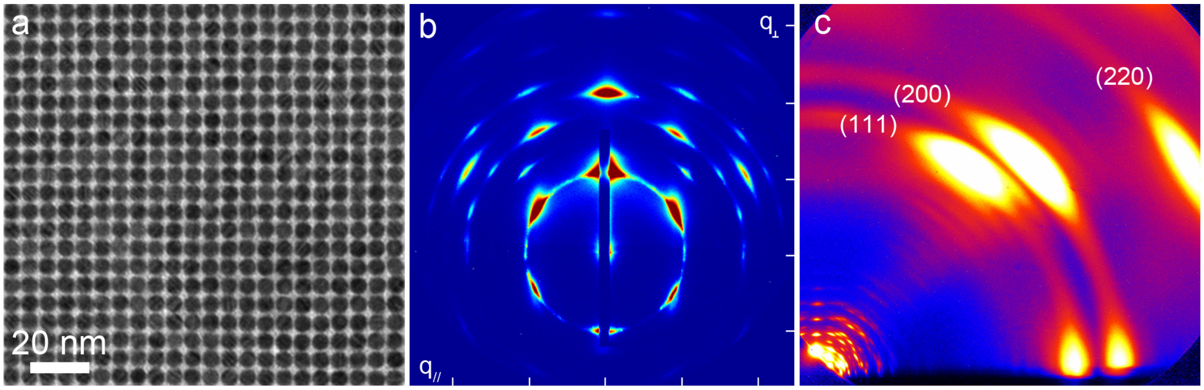

▲ Figure 1: a) Transmission electron micrograph of a QD superlattice. b) Grazing-incidence small-angle X-ray scattering pattern for a large-area (1x1 cm) film of the QDs. The peak locations index to that of a body-centered cubic superlattice. c) Wide-angle X-ray scattering pattern showing that the atomic planes of the QDs are aligned for the same sample used in (b). Atomic planes are labeled in white.

## FURTHER READING

- P. Guyot-Sionnest, "Electrical Transport in Colloidal Quantum Dot Films," *The Journal of Physical Chemistry Letters*, vol. 3, pp. 1169-1175, 2012.
- J. Choi, C. Bealing, K. Bian, K. Hughes, W. Zhang, D. Smilgies, R. Hennig, J. Engstrom, and T. Hanrath, "Controlling Nanocrystal Superlattice Symmetry and Shape-Anisotropic Interactions through Variable Ligand Surface Coverage," *Journal of the American Chemical Society*, vol. 133, pp. 3131-3138, 2011.

# Using Self-Assembled Block Copolymer Patterns to Template Bilayer Mesh Structures

A. Tavakkoli K.G., S.M. Nicaise, W. Bai, C.A. Ross, K.K. Berggren

Sponsorship: SRC, FENA Center, National Science Foundation, TSMC

Mesh-shaped patterns are needed for applications such as metamaterials and next-generation integrated circuit architecture in which high throughput of dense features will be required. Our previous studies showed that with arrays of majority-functionalized posts fabricated by electron-beam lithography (EBL), we controlled bilayers of block copolymer (BCP) cylindrical microdomains and fabricated a variety of complicated structures including mesh-shaped patterns. This work required EBL fabrication, difficult in a large-area manufacturing process. In the current study we investigated an EBL-free process for fabricating bilayer mesh structures. We used BCP patterns as templates to self-assemble another BCP layer of the same or different molecular weight, the latter on top of the former.

Figure 1 describes the main steps of the fabrication process. In the first step, poly(styrene-dimethylsiloxane) (PS-PDMS) BCP was spin-coated on the surface of a silicon substrate. Thermal or solvent annealing was used to promote microphase separation and reactive ion etch (RIE) was used to remove the PS matrix and leave the pattern. Next the second layer of PS-PDMS BCP was spin-coated on the patterns and self-assembled with annealing. Finally, RIE removed the PS matrix and left a mesh-shaped bilayer cylinder structure.

Figure 2 (c) shows one of the results of the described process. In this figure, a bilayer rectangular mesh-shaped structure was formed using a 53 kg mol$^{-1}$ PS-PDMS, as in Figure 2(b), on top of a 16 kg mol$^{-1}$ PS-PDMS, as in Figure 2(a). In other systems, BCPs have been shown to orient perpendicular to underlying periodic patterns because the free energy for perpendicular orientation of the second BCP to the bottom pattern is lower than parallel orientation. The layers in Figure 2(c) are not orthogonal all across the substrate because the bottom BCP pattern was poorly oriented. In order for the mesh to be orthogonal, the bottom BCP pattern can be templated.

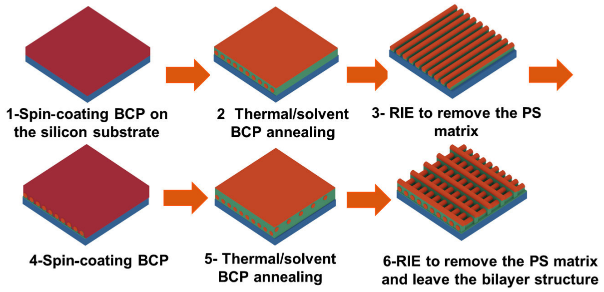

▲Figure 1: The major steps of bilayer mesh-shaped structure fabrication.

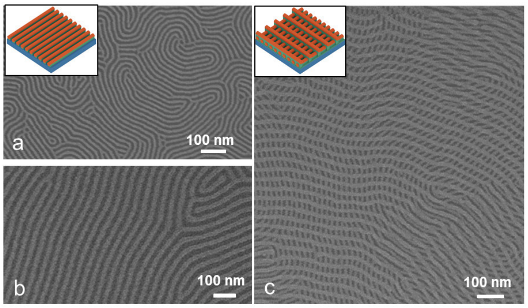

▲Figure 2: SEM images of (a) single layer of cylinders from 16 kg mol$^{-1}$ PS-PDMS BCP on silicon substrate, (b) single layer of cylinders from 53 kg mol$^{-1}$ PS-PDMS BCP on silicon substrate, (c) bilayer of 53 kg mol$^{-1}$ PS-PDMS on 16 kg mol$^{-1}$ PS-PDMS cylinders.

---

## FURTHER READING

- A. Tavakkoli K. G., K. W. Gotrik, A. F. Hannon, A. Alexander-Katz, C. A. Ross, and K. K. Berggren, Templating three-dimensional self-assembled structures in bilayer block copolymer films, *Science*, 2012, vol. 336, p. 1294.
- S. W. Hong, J. Huh, X. Gu, D. H. Lee, W. H. Jo, S. Park, T. Xu, and T. P. Russell, Unidirectionally aligned line patterns driven by entropic effects on faceted surfaces, *Proc. National Academy of Sciences*, 2012, vol. 109, p. 1402.

# Three-Dimensional Nanofabrication Using HSQ/PMMA Bilayer Resists

H. Do, J. Chang, K.K. Berggren

Sponsorship: Taiwan Semiconductor Manufacturing Company, National Science Foundation

Three-dimensional (3D) devices offer unique advantages over planar devices but are difficult to fabricate. Therefore, a simple and rapid fabrication process for complex 3D nanostructures is necessary. Methods for fabricating such 3D nanostructures using electron-beam lithography (EBL) include consecutive overlay exposures or low and high electron energy exposures. However, these approaches require alignment markers and accurate alignment routines. Here, we describe a self-aligned method of fabricating 3D nanostructures using EBL of hydrogen silsesquioxane (HSQ) and poly(methylmethacrylate) (PMMA).

We used a HSQ/PMMA bilayer resist stack with HSQ as the top layer and PMMA as the negative-tone bottom layer. A dot array was exposed on the bilayer resist stack with the dose necessary to achieve negative-tone PMMA. After exposure, the samples were sequentially developed in salty developer to remove unexposed HSQ, methyl isobutyl ketone (MIBK) and isopropanol (IPA) to remove lightly exposed PMMA, and acetone to remove unexposed PMMA. As shown in Figure 1(a-b), a nanostructure with larger diameter HSQ posts on top of smaller diameter PMMA posts was created due to the sensitivity difference between the two resists. The diameter of both posts was determined by the single dot exposure dose and the posts achieved vertical self-alignment. As shown in Figure 1(c), neighboring HSQ posts merged and formed wavy lines on top of PMMA posts when the dots were positioned sufficiently close to each other.

To better control the size and shape of the nanostructures on each resist layer, we developed a double exposure process in which smaller features on the bottom PMMA layer were defined using high dose exposures. Larger features on the top HSQ layer were defined using low dose exposures. Both layers were exposed in a single writing step without removing the wafer. Nanostructures similar to those shown in Figure 1(a-c) can be created in this method with more control by separately exposing the two resist layers. Figure 2(a-b) shows HSQ posts on top of PMMA posts and HSQ lines on top of PMMA posts, respectively. Because features on each resist layer can be more accurately controlled using this approach, complex 3D nanostructures can be fabricated as shown in Figure 2(c).

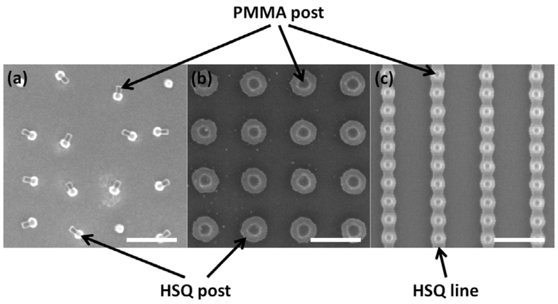

▲ Figure 1: SEM images of 3D nanostructures fabricated from single dot exposure. All scale bars are 200 nm long. (a) HSQ posts on top of PMMA posts. Collapsed nanostructures clearly show the two resist materials. (b) HSQ posts on PMMA posts. Exposure dose in (b) is 5.65 times the exposure dose in (a). (c) HSQ lines on PMMA posts.

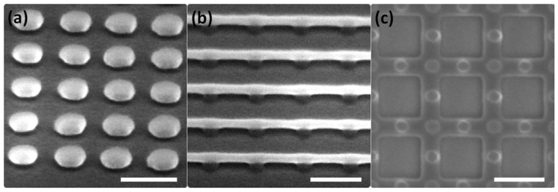

▲ Figure 2: SEM images of 3D nanostructures fabricated from double exposure process. SEM images (a) and (b) at 45° tilt angle. Exposure dose of negative-tone PMMA was 7 times exposure dose of HSQ. Scale bars are 100 nm (a-b) and 200 nm (c). (a) HSQ posts on top of 30-nm-diameter PMMA posts. (b) 60-nm-wide free-standing HSQ lines on 30-nm-diameter PMMA posts. (c) 75 nm wide HSQ grid on 50-nm-diameter PMMA posts.

## FURTHER READING

- J. Vila-Comamala, S. Gorelick, V. A. Guzenko, and C. David, "3D nanostructuring of hydrogen silsesquioxane resist by 100 keV electron beam lithography," *J. Vac. Sci. Technol. B* vol. 29, p. 06F301, 2011.
- E. J. Boyd and R. J. Blaikie, "Three-dimensional HSQ structures formed using multiple low energy electron beam lithography," *Microelectron. Eng.* vol. 83, pp. 767-770, 2006.

# High-Resolution Templated Hydrothermal Growth of ZnO Nanowires

S.M. Nicaise, A. Kiani, J.J. Cheng, S. Gradecak, K.K. Berggren
Sponsorship: MIT Energy Initiative

Zinc oxide nanowires (ZnO NWs) with uniform growth geometries (size, orientation, and pitch) can be grown perpendicular to a ZnO seed-layer thin film via the low-temperature hydrothermal process. In ZnO NW/quantum dot (QD) photovoltaics where NW growth geometry impacts device performance, an ideal NW pitch of 276 nm, similar to the depletion region width, optimizes performance. To control NW pitch as well as analyze other geometric characteristics, we fabricated poly(methyl methacrylate) (PMMA) masks that templated NW growth, Figure 1 shows a key example. While templated ZnO NW growth has been previously reported, this work specifically achieved high-resolution templating on various substrates and analyzed PV-specific geometric characteristics. This work could potentially improve QD infiltration into the NW array and increase exciton extraction efficiency.

Figure 2 shows the major steps of the fabrication process. The ZnO seed layers were spin- and RF-sputtercoated on silicon, indium-tin-oxide-coated glass, and polyethyleneimine substrates. Templating hole arrays were patterned in PMMA via electron-beam lithography. The hole arrays templated the hydrothermal growth of the ZnO NWs so that NWs grew only through the holes. We improved NW alignment and reduced branching by experimentally varying template hole diameter from 30-230 nm. NW alignment (orthogonal to the surface) was measured by the order parameter and found to increase with larger templating hole diameters. In contrast, NWs exhibited less branching for smaller hole diameters. More generally, overall branching was reduced when seed layers were thermally annealed. Atomic force microscopy showed increased grain sizes for annealed seed layers, suggesting an approach to offset branching. This investigation can be applied to improve the photocurrent in ZnO NW/QD PVs, as well as the performances of other ZnO NW-based devices.

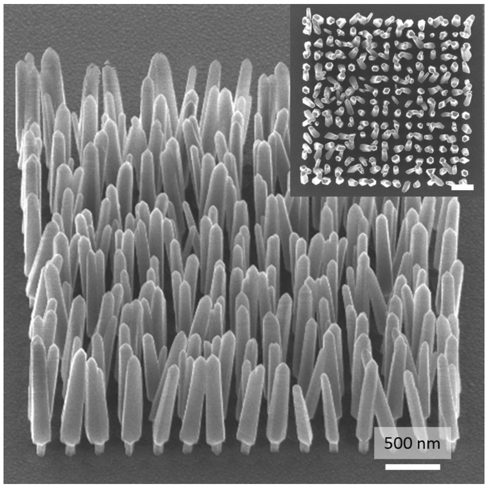

▲Figure 1: Scanning helium-ion micrograph (45° and top-down) of templated ZnO NW array. NWs were hydrothermally grown through PMMA hole templates (pitch 276 nm). This example is from unannealed, sputtered ZnO on Si. Branching is negligible; NWs are predominantly perpendicularly aligned.

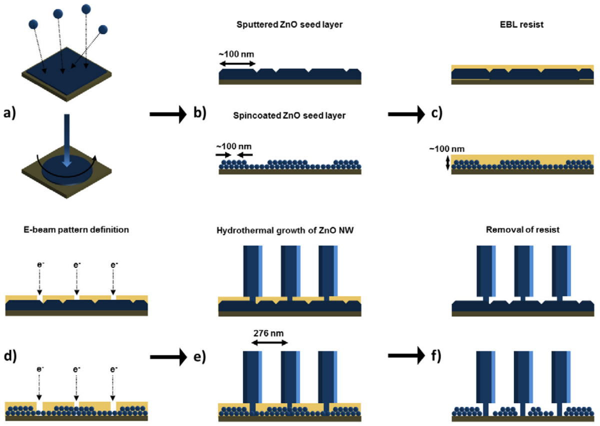

▲Figure 2: Experimental steps (schematics): a) ZnO seed layer deposited by sputtering (top) or spin-coating (bottom), b) optional annealing at 400°C for 2 hours, c) PMMA resist spin-coated and d) templating holes by EBL, e) NWs hydrothermally grown through template, and f) plasma etching removed PMMA. Grey- substrate, blue -ZnO, green -PMMA.

## FURTHER READING

- H. Park, S. Chang, J. Jean, J. J. Cheng, P. T. Araujo, M. Wang, M. Bawendi, M. S. Dresselhaus, V. Bulović, J. Kong, and S. Gradečak, "Graphene cathode-based ZnO nanowire hybrid solar cells," *Nano Letters* vol. 13, pp. 233-239, 2013.
- J. Jean, S. Chang, P. R. Brown, J. J. Cheng, P. H. Rekemeyer, M. G. Bawendi, S. Gradecak, and V. Bulović, "ZnO Nanowire Arrays for Enhanced Photocurrent in PbS Quantum Dot Solar Cells,"*Advanced Materials*, vol. 25, pp. 2790-2796, 2013.
- V. R. Manfrinato, D. D. Wanger, D. B. Strasfeld, H.-S. Han, F. Marsili, J. P. Arrieta, T. S. Mentzel, M. G. Bawendi, and K. K. Berggren, "Controlled placement of colloidal quantum dots in sub-15-nm clusters," *Nanotechnology* vol. 24, p. 125302, 2013.

# Ultrafast Plasmonic Au Nanorod Array Photocathodes

Y. Yang, R. Hobbs, W. Putnam, P. Keathley, E. De Leo, W. Graves, F. Kärtner, K.K. Berggren
Sponsorship: DARPA, Gordon and Betty Moore Foundation

High-density arrays of optically actuated nanoscale electron emitters can facilitate the development of ultrafast and high-brightness photocathodes for the next-generation free-electron lasers (FELs). The emitters can also find applications in time-resolved electron microscopy, crystallography, and spectroscopy Optical near-field enhancement due to localized surface plasmon resonance in metallic nanoparticles generates strong surface fields localized on the nanoscale. These fields are a prerequisite for high-brightness electron sources to minimize the area of electron emission and thus increase the source brightness. Surface-plasmon-enhanced photocathodes with femtosecond pulsed optical switches will enable the development of electron and X-ray analysis of materials with unparalleled spatial and temporal resolution.

In this work, we fabricated arrays of plasmonic Au nanorods with critical dimensions below 20 nm via electron beam lithography and metal lift-off on a sapphire substrate sputter-coated with indium-doped tin oxide (ITO) thin film. We have excited electron emission from Au nanorod arrays using ultrafast pulses of 800-nm light, with pulse durations as short as 7 fs,and repetition rates as high as 84 MHz. We measured the emission current from these photocathodes as a function of incident laser-pulse energy, applied static field, and nanorod array density. Transition from a multiphoton absorption process to strong-field tunneling process in the emission mechanism with increasing laser intensity has been observed, as were space-charge effects with increasing emission current, *e.g.*, linear scaling of emission current with applied static field. The timescale of the emission process was investigated by interferometric autocorrelation, and the emission was shown to be both prompt and on the timescale of the femtosecond optical pulse used to excite emission. Consequently, arrays of optically actuated, surface-plasmon-enhanced Au nanorod electron emitters are promising candidates for applications in high-brightness, ultrafast electron, and X-ray sources.

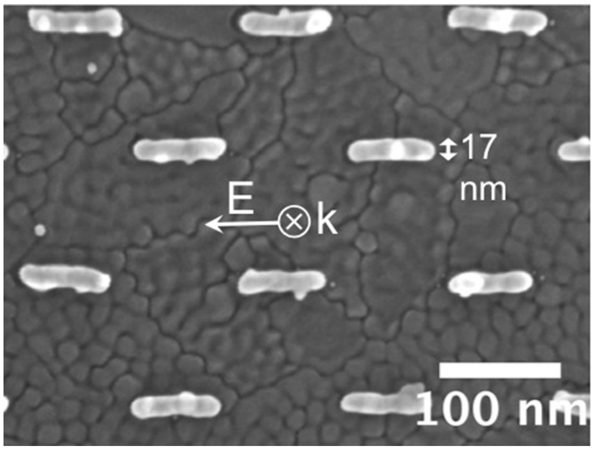

▲Figure 1: SEM image of Au nanorod array on 80-nm film of ITO on a sapphire substrate. Orientation of linear polarization (E) of light used to excite electron emission is depicted by arrow, as is direction of light propagation (k) into plane of ITO film.

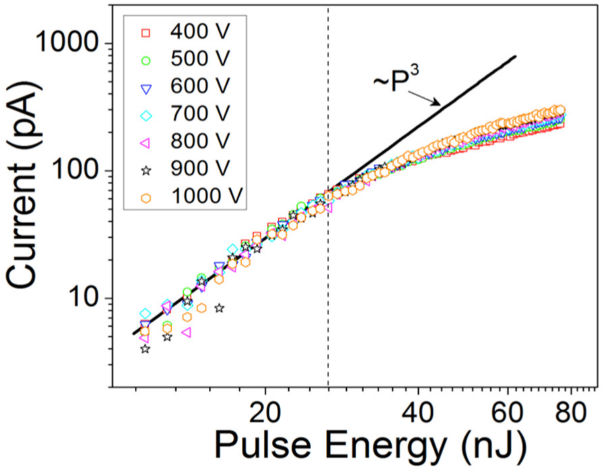

▲Figure 2: Emission current vs. pulse energy at various anode bias values for a 1-μm pitch square array of Au nanorods illuminated by a 90-μm (FWHM) beam of 35 fs pulses of 800-nm light (3 kHz rep. rate).

---

## FURTHER READING

- W. S. Graves, F. X. Kärtner, D. E. Moncton, and P. Piot, "Intense superradiant x rays from a compact source using a nanocathode array and emittance exchange," *Physical Review Letters*, vol. 108, no. 26, p. 263904, 2012.
- A. Polyakov, C. Senft, K. F. Thompson, J. Feng, S. Cabrini, P. J. Schuck, and W. P. Hess, "Plasmon-enhanced photocathode for high brightness and high repetition rate X-ray sources," *Physical Review Letters*, vol. 110, no. 7, p. 076802, 2013.
- P. Dombi, A. Hörl, P. Rácz, I. Márton, A. Trügler, J. R. Krenn, and U. Hohenester, "Ultrafast strong-field photoemission from plasmonic nanoparticles," *Nano Letters*, vol. 13, no. 2, pp. 674-678, 2013.

# Determining the Resolution Limits of Electron-Beam Lithography

V.R. Manfrinato, J. Wen, L. Zhang, Y. Yang, R. Hobbs, B. Baker, D. Su, D. Zakharov, N.J. Zaluzec, D.J. Miller, E.A. Stach, K.K. Berggren

Sponsorship: Center for Excitonics (DOE), Brookhaven National Laboratory, Argonne National Laboratory

Electron-beam lithography (EBL) exposure starts with a focused electron beam that deposits energy locally in the resist. This electron beam can also excite secondary electrons (SEs), plasmons, phonons, and photons that may further deposit energy (or break bonds) in the resist. These excited particles deposit energy away from the direct beam and may lead to loss in resolution. Since the invention of EBL 50 years ago, all the mechanisms that lead to the final energy distribution in the resist, that is, the lithographic point-spread function (PSF), are not quantitatively clear. The PSF is the primary metric to understand the resolution limits of the EBL exposure step. The SEs have been considered to be the largest contributors to the lithographic PSF. The role of SEs on EBL has been extensively modeled, but it has not been directly measured to date. Furthermore, the role of plasmons on SE emission has been extensively studied, but the plasmon effect on EBL has not been experimentally investigated. Figure 1a shows the direct-beam PSF (blue), which is the spatial energy density deposited by the direct (or forward-scattered) electron beam in the resist. The direct-beam PSF was measured using chromatic-aberration-corrected energy-filtered transmission electron microscopy. From the direct-beam PSF to the lithographic PSF, we have the total effect of delocalized energy transfer in EBL. Figure 1a shows the measured volume-plasmon (VP) PSF (green), which is the spatial energy density deposition caused by VPs in the resist. We determined the VP PSF by calculating the dielectric constant of the resist at the VP energy (22.5 eV) from electron energy loss spectroscopy. Furthermore, we performed Monte Carlo simulations of the PSF. From Figure 1a we observed that the direct-beam PSF is the largest component for sub-2-nm radius and the VP PSF dominates for radius larger than 2 nm. In Figure 1b we combined the VPs and SEs PSFs by weighting the energy loss of each process. The measured energy loss from VPs was 35% of the total loss. We concluded that VPs were the largest energy loss mechanism in the lithographic PSF, limiting the EBL resolution.

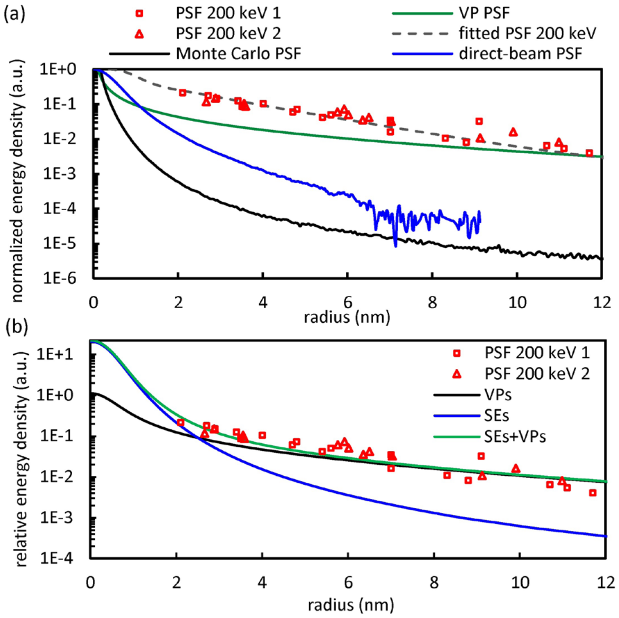

Figure 1: (a) Components of lithographic PSF (maximum value of all PSFs set to unity): (blue) direct-beam PSF, (green) VP PSF, (black) lithographic PSF by Monte-Carlo simulation including SEs, (gray) fitted lithographic PSF, and (red squares - dataset 1 - and red triangles - dataset 2) lithographic PSF from dot-exposure method. (b) (blue) deposited energy density due to SEs, calculated from Monte-Carlo lithographic PSF including SEs and instrument spot size; (black) deposited energy density due to VPs, calculated from VP PSF and direct-beam PSF for energies <50 eV; and (green) total deposited energy density. Lithographic PSF was overlaid with total deposited energy density. The VPs were necessary to match total deposited energy density to lithographic PSF.

---

## FURTHER READING

- H. Duan, V. R. Manfrinato, J. K. W. Yang, D. Winston, B. M. Cord, and K. K. Berggren, "Metrology for electron-beam lithography and resist contrast at the sub-10nm scale," *Journal of Vacuum Science and Technology B*, vol. 28, pp. H11-H17, 2010.
- V. R. Manfrinato, L. Zhang, D. Su, H. Duan, R. G. Hobbs, E. A. Stach, and K. K. Berggren, "Resolution limits of electron-beam lithography towards the atomic scale," *Nano Letters*, vol. 13, pp. 1555–1558, 2013.
- V. R. Manfrinato, J. Wen, L. Zhang, Y. Yang, R. G. Hobbs, B. Baker, D. Su, D. Zakharov, N. J. Zaluzec, D. J. Miller, E. A. Stach, and K. K. Berggren, "Determining the resolution limits of electron-beam lithography: direct measurement of the point-spread function," *Nano Letters*, 2014, DOI: 10.1021/nl5013773.

# Non-demolition Quantum Electron Microscope in Free-space

C.S. Kim, Y. Yang, V.R. Manfrinato, R.G. Hobbs, K.K. Berggren, P. Kruit
Sponsorship: GBMF

Electron microscopy (EM) has significantly influenced many areas of science and engineering due to its unprecedented atomic resolution. However, the imaging of biological samples has been restricted by sample damage induced by energetic electrons. Despite advances in hydrated environmental chambers, samples still experience physical and chemical damages due to exposure to energetic electrons. In 2009, a quantum electron microscope (QEM) was proposed consisting of two quantum-mechanically coupled electron ring resonators.

We are interested in proof-of-concept of QEM. Thus, we have designed the concept of a free-space QEM based on two electron rings where the electron wavefunction in the two rings is coupled via a diffractive crystal (Figure 1). The diffractive crystal acts to split the incident electron beam into a reference beam and a sample beam, both of which undergo many circulations (100 times) through the coupler to achieve the goal of reduced sample damage as shown in Figure 1.

For diffractive couplers, we used focused Ga and He ion beams to fabricate ~ 10-nm-thick silicon and diamond crystal membranes. We have investigated the impact of the ion beams on the crystal structure of the membranes. Additionally, we have studied decoherence effects induced by the couplers using electron energy loss spectroscopy and simulation. As a first step toward a proof-of-concept non-demolition QEM, we fabricated a linear series of couplers from a single Si crystal and successfully demonstrated (Figure 2) coherent coupling was successfully demonstrated (Figure 2).

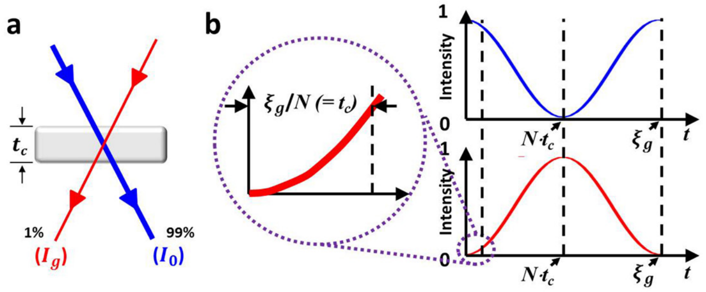

◀Figure 1: Non-demolition microscope concept. `(a) Electron rings (red: sample ring, blue: reference ring) overlap in real space and are coupled at a diffractive crystal by Bragg diffraction. (b) Intensity in reference ring ($I_o=cos^2(\pi\times t_c/\xi_g)$) oscillates as a function of crystal thickness; tc is thickness of crystal and xg is extinction distance. Intensity in sample ring decays commensurate with increase in intensity in reference ring ($I_g=sin_2(\pi\times t_c/\xi_g)$). In QEM, each electron undergoes N circulations through coupler as shown.

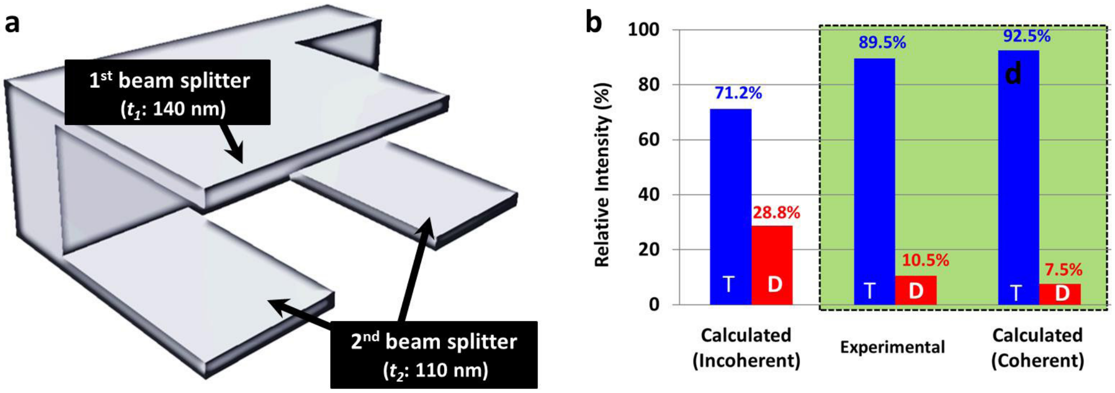

▲Figure 2: Multiple diffraction-based coupler: (a) Geometry of serial coupler with two thin crystal membranes fabricated from one crystal, thus keeping same crystal orientation in both splitters. Incident electron experiences two successive splitting events by 1st and 2nd beam splitter; (b) Relative intensity in calculation and experiment compared for transmitted vs. diffracted beams.

## FURTHER READING

- R. Glaeser and K. Taylor, *J. Microsc.* vol. 112, p. 127, 1978.
- W. P. Putnam and M. F. Yanik, *Phys. Rev. A* vol. 80, p. 040902R, 2009.

# Designing Lubricant-Impregnated Textured Surfaces to Resist Scale Formation

S.B. Subramanyam, G. Azimi, K.K. Varanasi
Sponsorship: MIT Energy Initiative

Scale formation or mineral scale fouling is a widespread problem in industries and households, from the scaling of cooking pots in ancient times to the plugging of pipelines in the modern age. For example, in an oil well in the North Sea, scale formation resulted in a shocking loss of production from 30,000 barrels/day to zero in just 24 hours. It is also estimated that the costs due to fouling of heat exchangers in the United States is about 0.2% - 0.25% of the nation's GNP. Scale deposits reduce process efficiency, increase production costs, lead to under-deposit corrosion, and are centers of radioactivity. The current technologies to address this problem using chemical inhibitors or mechanical/chemical methods of removal are ineffective, energy-intensive, or environmentally unfriendly. Developing surfaces that have a low affinity to scale has been an area of great interest in the last decade.

In this work, we demonstrate the anti-scaling properties of textured surfaces impregnated with a lubricant. The lubricant is stabilized by the capillary forces exerted by the micro/nano features of the solid substrate. From the classical nucleation theory, it is known that reducing the surface energy and the roughness of the substrate reduces the nucleation rate of scale or salt on the surface and hence the overall scale deposition. We optimize the design of the lubricant-impregnated surfaces (LIS) based on the surface tension of the lubricant and its spreading coefficient on the solid. The use of a low-surface-tension spreading liquid as the impregnating lubricant renders the surface extremely smooth and lowers its surface energy. Scale deposition experiments show that the overall scale formation on LIS is reduced owing to their smooth, low-energy surfaces (as in Figure 1). Mass gain measurements indicate that the optimized LIS perform 10 times better than uncoated smooth surfaces (as Figure 2 shows). We extend this idea to an engineering material like stainless steel and show that along with low scale deposition, we also achieve low adhesion of scale to LIS.

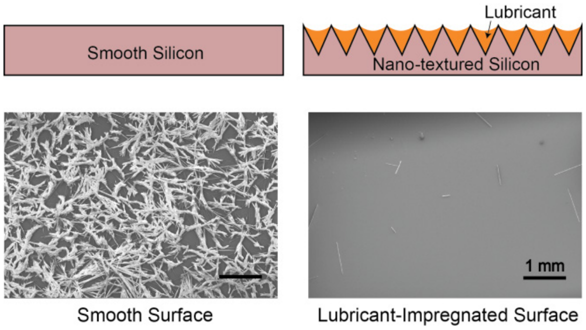

▲ Figure 1: Comparison of gypsum scale formation on a smooth silicon surface (left) and a lubricant-impregnated surface LIS (right) after ~80 hours of residence time in a saline solution.

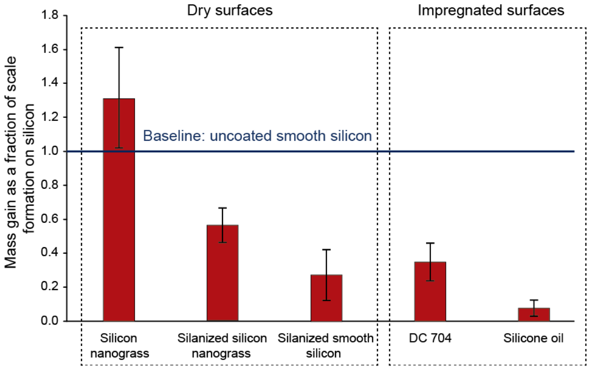

▲ Figure 2: Mass gain due to calcium sulfate formation after the substrates were immersed in the salt solution for ~80 hours, expressed as a fraction of the mass gain on silicon.

## FURTHER READING

- S. B. Subramanyam, G. Azimi, and K. Varanasi, "Designing Lubricant-Impregnated Textured Surfaces to Resist Scale Formation" *Advanced Materials Interfaces*, vol. 1, p. 1300068, 2014.
- S. B. Subramanyam, K. Rykaczewski, and K. Varanasi, "Ice Adhesion on Lubricant-Impregnated Surfaces" *Langmuir*, vol .29, pp. 13414-13418, 2013.
- J.D. Smith, R. Dhiman, S. Anand, E. Reza-Garduno, R. Cohen, G. McKinley, and K. Varanasi, "Droplet Mobility on Lubricant Impregnated Surfaces," *Soft Matter*, vol. 9, pp. 1772-1780, 2012.

# Ice Adhesion on Lubricant-Impregnated Textured Surfaces

S.B. Subramanyam, K. Rykaczewski, K.K. Varanasi

Sponsorship: MIT Energy Initiative, Doherty Chair in Ocean Utilization

From aircrafts to wind farms, incidents due to excessive ice buildup have threatened human safety and the efficient functioning of energy and transportation systems for many decades. Current efforts of addressing this problem focus on the removal of accumulated ice using a variety of established de-icing methods. However, these approaches are inefficient, expensive and in some cases environmentally unfriendly. Passive approaches such has surfaces that have a strong ice-repellant nature are becoming increasingly important.

One of the ways of quantifying the anti-icing properties of a surface is by measuring the adhesion of ice to the surface. Here, we study the ice-adhesion properties of Lubricant-Impregnated Surfaces (LIS) – micro/nano textured surfaces imbibed with a liquid lubricant. Force measurements show ice adhesion strength on textured surfaces impregnated with thermodynamically stable lubricant films to be higher than that on surfaces with excess lubricant. The excess lubricant, although resulting in a lower ice adhesion, is unstable and can easily be washed away due to external forces like drag, gravity etc. Hence the optimization of LIS is important to attain superior performance compared to the conventional surface treatments.

Systematic ice-adhesion measurements indicate that the ice-adhesion strength is dependent on texture and decreases with increasing texture density. Direct cryogenic SEM imaging of the fractured ice surface and the interface between ice and lubricant-impregnated textured surface (Figure 1) reveal stress concentrators and crack initiation sites that can increase with texture density and result in lowering adhesion strength. Figure 2 shows a comparison of the ice adhesion strength on different surface treatments. The plot compares a smooth silane coating, a fluoroPoss based coating and LIS with the highest texture density. Thus, lubricant-impregnated surfaces have to be optimized to outperform state-of-the-art icephobic treatments.

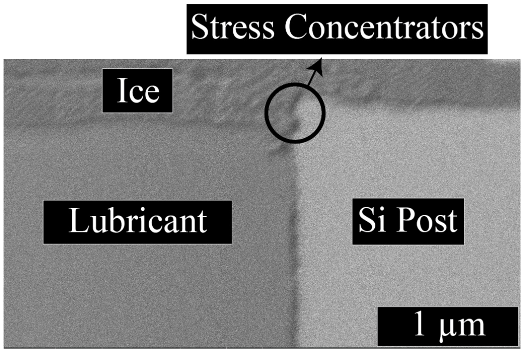

▲ Figure 1: FIB-cross-section of the interface between ice and LIS under cryogenic conditions. The SEM image indicates the presence of stress concentrator that act as crack nucleation sites.

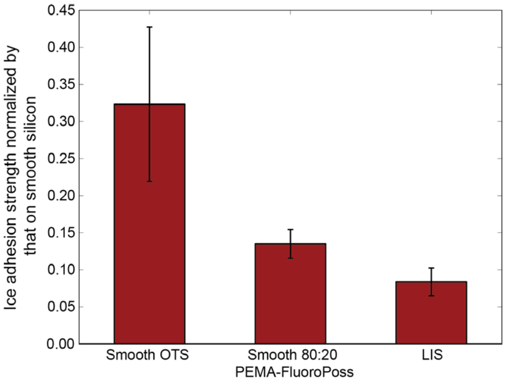

▲ Figure 2: Comparison of ice adhesion strength on state-of-the-art surfaces – a smooth silane coated surface (OTS), a smooth 80:20 PEMA-FluroPoss coated surface and a Lubricant-Impregnated Surface with the highest texture density.

## FURTHER READING

- S. B. Subramanyam, K. Rykaczewski and K. Varanasi "Ice Adhesion on Lubricant-Impregnated Surfaces" *Langmuir*, vol.29, pp. 13414-13418, 2013.
- J.D. Smith, R. Dhiman, S. Anand, E. Reza-Garduno, R. Cohen, G. McKinley and K. Varanasi "Droplet Mobility on Lubricant Impregnated Surfaces" *Soft Matter*, vol. 9, pp. 1772-1780, 2013
- S. B. Subramanyam, G. Azimi and K. Varanasi "Designing Lubricant-Impregnated Textured Surfaces to Resist Scale Formation" *Advanced Materials Interfaces*, vol.1, p. 1300068, 2014.
- K. Rykaczewski, S. Anand, S. B. Subramanyam and K. Varanasi "Mechanism of Frost Formation Lubricant Impregnated Surfaces" *Langmuir*, vol. 29, pp. 5230-5238

# Enhanced Condensation Heat Transfer on Grafted Polymer Films Via iCVD

A.T. Paxson, J.L. Yagüe, K.K. Gleason, K.K. Varanasi

Sponsorship: US Army Research Office, National Science Foundation

Roughly 85% of the global electricity install base and 50% of desalination plants worldwide rely on steam condensers. Given the massive scale of these processes, any improvements in cycle efficiencies would have a profound effect on global energy consumption. Dropwise condensation has been an active area of research for nearly a century, as the resulting heat transfer coefficients can be an order of magnitude higher than those seen in filmwise condensation. However, the practical implementation of this concept in power generation, desalination, and other applications has been a significant materials challenge, limited by durability of existing hydrophobic functionalization for metal heat transfer surfaces. Metallic heat transfer surfaces must be modified with a hydrophobic coating to obtain dropwise condensation, but because the thermal conductivities of polymeric materials are typically orders of magnitude smaller than that of a metal substrate, it is crucial that a polymer modifier be as thin as possible to minimize thermal resistance. Hence, there is a need for an ultra-thin robust hydrophobic modifier.

We have recently demonstrated the sustained dropwise condensation of steam on a thin film of poly-(1H,1H,2H,2H-perfluorodecyl acrylate)-*co*-divinyl benzene p(PFDA-*co*-DVB) covalently grafted to a metal substrate by initiated chemical vapor deposition (iCVD). The iCVD process is a single-step, solvent-free, low-energy, vapor-phase method used to deposit conformal films with precisely controllable thickness. Briefly, monomer and initiator species (Figure 1a) are flowed into a reactor at controlled rates and encounter heated filaments and a cooled substrate. The locally heated zone around the filaments thermally cleaves the initiator species (tert-butyl peroxide, TBPO). The radical fragments produced initiate vinyl polymerization of the monomers absorbed on the surface to form semicrystalline agglomerations (Figure 1b, c).

Accelerated endurance tests were conducted by condensing steam at 100°C. Coatings of p(PFDA-*co*-DVB) were compared to fluorosilane coatings, both on aluminum substrates (Figure 2a, b). The grafted polymer coating exhibits dropwise condensation with a departing droplet size of 4.2 ± 0.1 mm and a heat transfer coefficient greater than 35 kW $m^{-2}$ $K^{-1}$, which is more than 7 times greater than the steady-state filmwise heat transfer coefficient of the degraded silanized surface, with no noticeable degradation after 48 hours of condensation (Figure 2c).

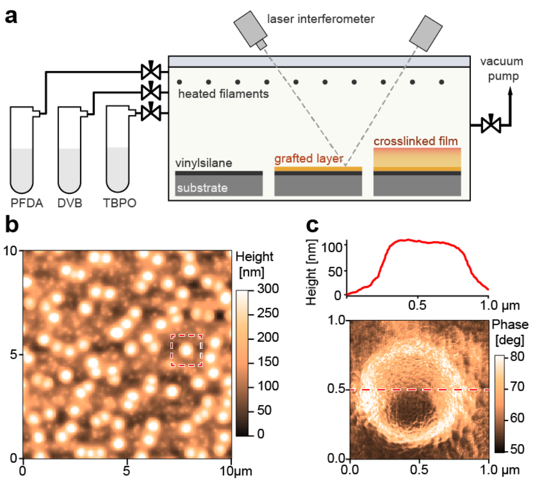

▲Figure 1: iCVD chamber geometry and deposition process (a). AFM images of rough copolymer surface consisting of hemispherical agglomerations (b); detail of semicrystalline agglomeration (c).

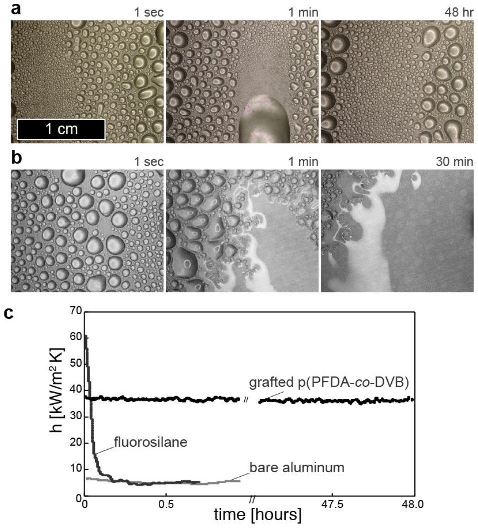

▲Figure 2: Sustained dropwise condensation on iCVD copolymer (a) vs. rapid degradation of fluorosilane coating (b). Plot of heat transfer coefficient vs time (c).

## FURTHER READING

- A. T. Paxson, J. L. Yagüe, K. K. Gleason, K. K. Varanasi, "Stable dropwise condensation or enhancing heat transfer via the initiated chemical vapor deposition (iCVD) of grafted polymer films," *Advanced Materials*, vol. 26, pp. 418-423, 2014.

# Fog-Harvesting Potential of Lubricant-Impregnated Electrospun Nanomats

B.S. Lalia, S. Anand, R. Hashaikeh, K.K. Varanasi
Sponsorship: MIT, Masdar Institute of Science and Technology

Hydrophobic PVDF-HFP nano-webs were fabricated by a facile electrospinning method and proposed for harvesting fog from the atmosphere. PVDF-HFP polymer was used to prepare electrospun nanomats due to its inherent hydrophobicity. As prepared electrospun nanomats show strong adhesive forces with water. The impregnation of lubricant in nano/micro-pores of nanomats dramatically lowers the retentive force between water droplets and nanomat surface indicated by the low contact angle hysteresis and promotes roll-off of small sized droplets. Impregnation of nanomats with lubricants (Total Quartz Oil and Krytox 1506) decreased the contact angle hysteresis and hence improved roll off of water droplets on the nanomats surface. It was found that water droplets of 5 µl size (dia.=2.1 *mm*) and larger roll down on an oil impregnated surface, held vertically, compared to 38 µl (dia.=4.2 mm) on plain nano-web. Contact angle hysteresis reduced from ~95° to ~23° with the Krytox 1506 impregnation (Figure 1). The prepared nanomats exhibit great potential to prepare stable lubricant impregnated surfaces due to their high porosity by virtue of which they wick large lubricant proportionate to their weight. The fog collection studies show that collection rates on the low hysteresis impregnated sample is higher than the water collection rates on the high hysteresis un-impregnated sample (Figure 2). Further we show that nanomats impregnated with the lubricant show significantly less drainage of oil from the surface along with shedding water.

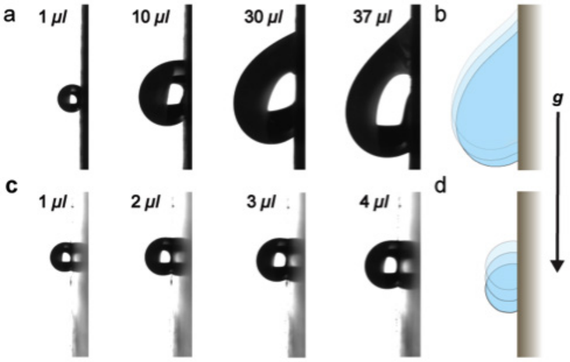

▲Figure 1: Optical images of different size water drops on the vertical surface of nanomat (a) and nanomat impregnated with Total Quartz Oil (c). Schematic of water drop sliding on the nanomat (b) and on the nanomat impregnated with Total Quartz Oil (d).

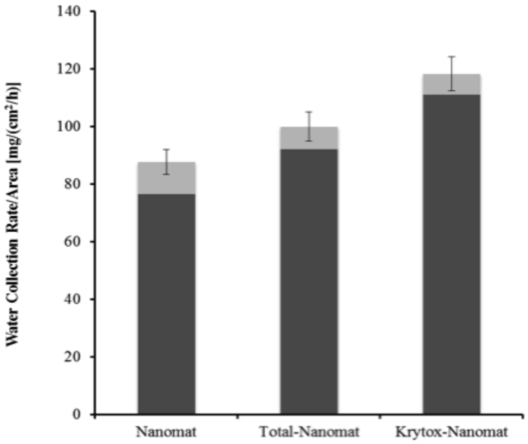

▲Figure 2: Fog collection behavior with time for nanomats with and without lubricant impregnation

## FURTHER READING

- Lalia, B. S.; Anand, S.; Varanasi, K. K.; Hashaikeh, R., "Fog-Harvesting Potential of Lubricant-Impregnated Electrospun Nanomats," *Langmuir* **2013,** *29* (42), 13081-13088.
- Rykaczewski, K.; Anand, S.; Subramanyam, S. B.; Varanasi, K. K., "Mechanism of Frost Formation on Lubricant-Impregnated Surfaces.,"*Langmuir* **2013,** *29* (17), 5230-5238.
- Smith, J. D.; Dhiman, R.; Anand, S.; Reza-Garduno, E.; Cohen, R. E.; McKinley, G. H.; Varanasi, K. K., "Droplet mobility on lubricant-impregnated surfaces.,"*Soft Matter* **2013,** *9* (6), pp 1772-1780.
- Anand, S.; Paxson, A. T.; Dhiman, R.; Smith, J. D.; Varanasi, K. K. ,"Enhanced Condensation on Lubricant-Impregnated Nanotextured Surfaces," *ACS Nano* **2012,** *6* (11), pp 10122-10129..
- Wong, T. S.; Kang, S. H.; Tang, S. K. Y.; Smythe, E. J.; Hatton, B. D.; Grinthal, A.; Aizenberg, J., "Bioinspired self-repairing slippery surfaces with pressure-stable omniphobicity," *Nature* **2011,** *477* (7365), pp 443-447.
- Lafuma, A.; Quéré, D. "Slippery pre-suffused surfaces," *EPL* **2011,** *96* (5), pp 56001.

# Mechanism of Frost Formation on Lubricant-Impregnated Surfaces

K. Rykaczewski, S. Anand, S.B. Subramanyam, K.K. Varanasi

Sponsorship: National Science Foundation Career Award, MIT Energy Initiative

Frost formation is a major problem affecting a variety of industries including transportation, power generation, construction, and agriculture. Currently used active chemical, thermal, and mechanical techniques of ice removal are time-consuming and costly. The use of nanotextured coatings infused with perfluorinated oil has recently been proposed as a simple passive anti-frosting and anti-icing method. However, we demonstrate that the process of freezing subcooled condensate and frost formation on such lubricant-impregnated surfaces is accompanied by the migration of the lubricant from the wetting ridge and from within the textured substrate to the surface of frozen droplets. For practical applications, this mechanism can comprise the self-healing and frost-repelling characteristics of lubricant impregnated-surfaces, regardless of the underlying substrate' s topography. Thus, further research is necessary to develop liquid-texture pairs that will provide a sustainable frost suppression method.

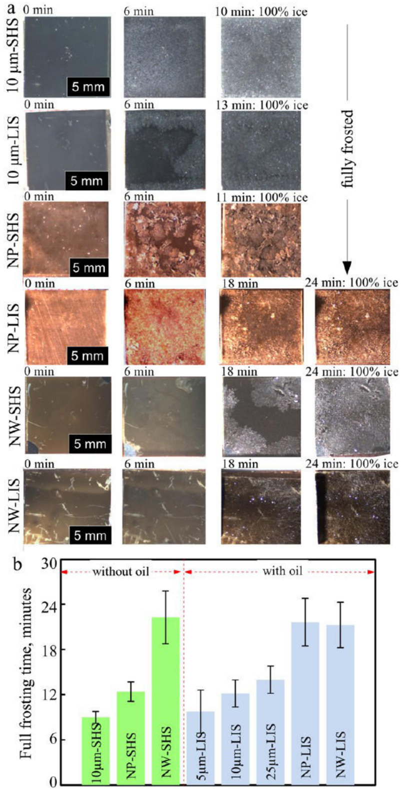

◀ Figure 1: (a) Example optical images of SHS and LIS samples from the beginning of cooling until full frost coverage. (b) Histogram of average times required for full sample frosting.

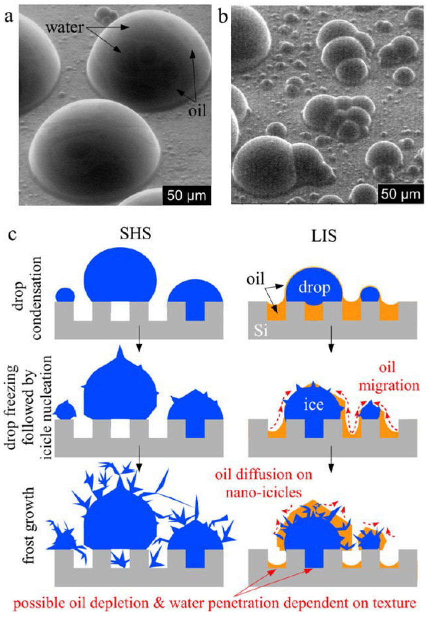

▶ Figure 2: ESEM images of (a) oil swirls on top of drops and (b) compound drops condensed on NP-LIS and schematic illustrations contrasting with (c) the mechanism of frost growth via drop condensation and freezing on SHS and LIS. (The extent of illustrated oil depletion and water penetration into the substrate is dependent on the length scale of the underlying texture.)

---

## FURTHER READING

- Rykaczewski, K.; Anand, S.; Subramanyam, S. B.; Varanasi, K. K. Mechanism of Frost Formation on Lubricant-Impregnated Surfaces. *Langmuir* **2013,** *29* (17), 5230-5238.
- Smith, J. D.; Dhiman, R.; Anand, S.; Reza-Garduno, E.; Cohen, R. E.; McKinley, G. H.; Varanasi, K. K. Droplet mobility on lubricant-impregnated surfaces. *Soft Matter* **2013,** *9* (6), pp 1772-1780.
- Anand, S.; Paxson, A. T.; Dhiman, R.; Smith, J. D.; Varanasi, K. K. Enhanced Condensation on Lubricant-Impregnated Nanotextured Surfaces. *ACS Nano* **2012,** *6* (11), pp 10122-10129..
- Kim, P.; Wong, T. S.; Alvarenga, J.; Kreder, M. J.; Adorno-Martinez, W. E.; Aizenberg, J. Liquid-infused nanostructured surfaces with extreme anti-ice and anti-frost performance. *ACS Nano* **2012,** *6* (8), pp 6569-6577.
- Wong, T. S.; Kang, S. H.; Tang, S. K. Y.; Smythe, E. J.; Hatton, B. D.; Grinthal, A.; Aizenberg, J. Bioinspired self-repairing slippery surfaces with pressure-stable omniphobicity. *Nature* **2011,** *477* (7365), pp 443-447.
- Lafuma, A.; Quéré, D. Slippery pre-suffused surfaces. *EPL* **2011,** *96* (5), pp 56001.
- Subramanyam, S. B.; Rykaczewski, K.; Varanasi, K. K. Ice adhesion on lubricant-impregnated textured surfaces. *Langmuir* **2013,** *29* (44), 13414-13418.
- Subramanyam, S. B.; Azimi, G.; Varanasi, K. K. Designing Lubricant-Impregnated Textured Surfaces to Resist Scale Formation. *Advanced Materials Interfaces* **2014,** *1* (2)

# Manufacturing of Freeform Carbon Nanotube Microstructures

M. De Volder, S.J. Park, S. Tawfick, A.J. Hart

Sponsorship: DARPA, Air Force Office of Scientific Research, Office of Naval Research

The skins of many plants and animals have intricate micro-scale surface features that give rise to properties such as directed water repellency and adhesion, resistance to fouling, and camouflage. However, engineered mimicry of these designs has been restrained by the limited capabilities of top-down fabrication processes.

We demonstrate a new technique for scalable manufacturing of freeform microstructures, via strain-engineered growth of aligned carbon nanotubes (CNTs). Offset patterning of the CNT growth catalyst is used to locally modulate the CNT growth rate. This causes the CNTs to collectively bend during growth, with exceptional uniformity over large areas. The final shape of the curved CNT microstructures can be designed via finite element modeling, and compound catalyst shapes produce microstructures with multi-directional curvature and unusual self-organized patterns. Because our process is based on an additive chemical synthesis process instead of a subtractive etching and release technique, it enables the direct synthesis of complex microstructures that are perpendicular rather than parallel to the substrate. This has two major implications: it enables fabrication of closely packed arrays of structures with heterogeneous shapes, and the porosity of the CNT forests enables conformal coating after growth to modify chemical and/or mechanical properties. We demonstrate this latter point by conformal coating of CNT "microtruss" arrays by atomic layer deposition (ALD) and polymer CVD, which increases their mechanical stiffness without changing the geometry. This process establishes versatile principles for design and manufacturing of complex microstructured surfaces that profit from the mechanical, electrical, and thermal properties of CNTs, and can leverage emerging methods for roll-to-roll micro-patterning and chemical vapor deposition.

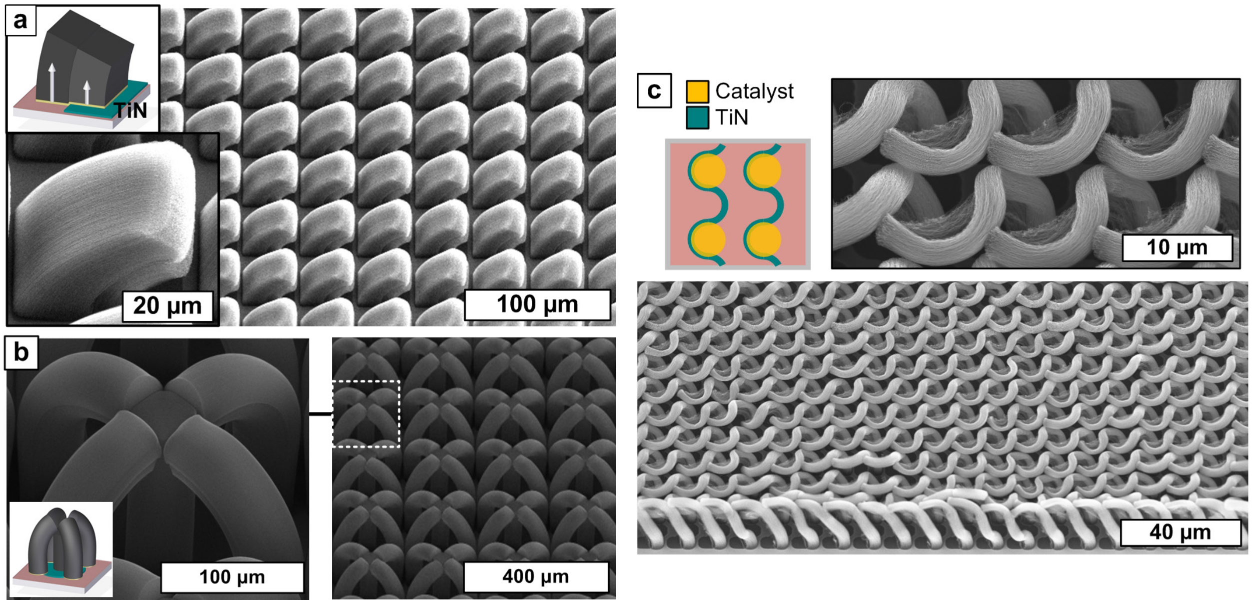

▲ Figure 1: Strain-engineered growth of 3D CNT microstructures by offset patterning of the growth catalyst on a TiN underlayer: (a) curved micropillars; (b) microtrusses; (c) self-organized woven texture.

## FURTHER READING

- M. De Volder, S.J. Park, S. Tawfick, A.J. Hart, "Strain-Engineered Manufacturing of Freeform Carbon Nanotube Microstructures. *Nature Communications (in press)*, 2014.

# Direct Fabrication of Graphene on Dielectric Substrates

D. McNerny, B, Viswanath, D. Copic, F. Laye, C. Prohoda, A. Brieland-Shoultz, E.S. Polsen, N.T. Dee, V.S. Veerasamy, A.J. Hart

Sponsorship: Guardian Industries, National Science Foundation, Air Force Office of Scientific Research

Recent advances in the growth of graphene by chemical vapor deposition (CVD) have enabled the controlled synthesis of graphene films of uniform thickness and high quality, despite their polycrystalline structure and orientation. To realize many of the potential applications of graphene, there remains a need for scalable methods of transferring graphene from the metal film or foil growth substrate, which is often Cu or Ni, to application-specific substrates. Moreover, graphene transfer methods typically require multiple steps, and can damage the graphene and/or degrade its properties such as electron mobility.

We demonstrate direct production of graphene on $SiO_2$ by CVD growth of graphene at the interface between a Ni film and the $SiO_2$ substrate, followed by dry mechanical delamination of the Ni using adhesive tape. This result is enabled by understanding of the competition between stress evolution and microstructure development upon annealing of the Ni prior to the graphene growth step. When the Ni film remains adherent after graphene growth, the balance between residual stress and adhesion governs the ability to mechanically remove the Ni after the CVD process. In this study the graphene on SiO2 comprises micron-scale domains, ranging from monolayer to multilayer. The graphene has >90% coverage across centimeter-scale dimensions, limited by the size of our CVD chamber. Further engineering of the Ni film microstructure and stress state could enable production of highly uniform interfacial graphene followed by clean mechanical delamination. With such understanding, this method could be scaled to manufacturing on wafer-scale and larger dimensions, either using blanket Ni films, or pre-patterned Ni shapes to directly template device geometries. Moreover, our findings suggest that preferential adhesion can enable production of 2-D materials directly on application-relevant substrates.

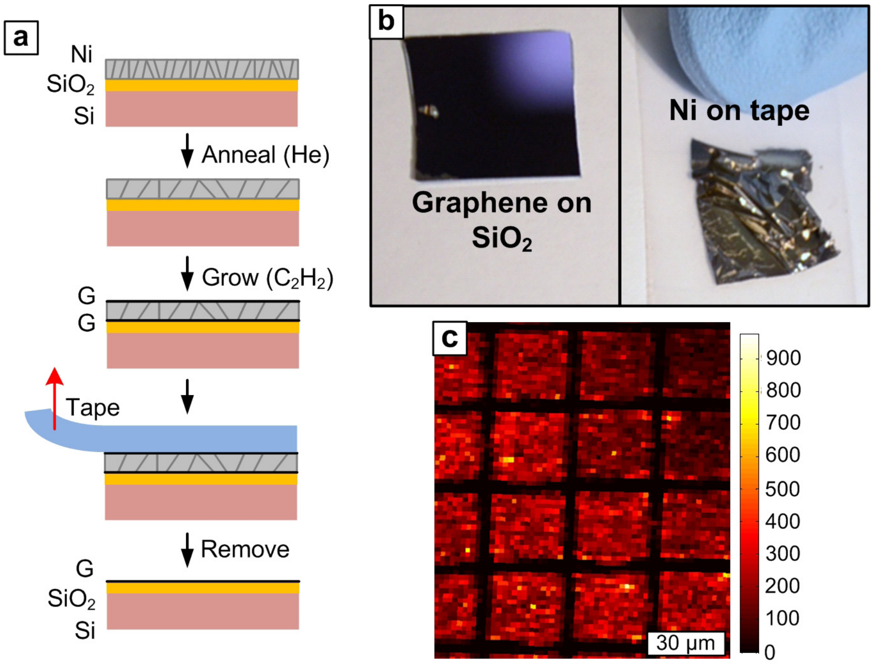

Figure 1: Direct fabrication of graphene on $SiO_2$ by interfacial growth followed by delamination of the Ni film a) Process schematic, indicating Ni grain growth during annealing in He, followed by graphene growth under CVD conditions, and then removal of Ni using adhesive tape. (b) Photo of substrates (~1×1 cm) and delaminated Ni films in case of ex situ tape delamination after graphene growth. (c) Two-dimensional Raman (G peak) intensity map of substrate with patterned graphene after Ni delamination.

## FURTHER READING

- D. McNerny, B, Viswanath, D. Copic, F. Laye, C. Prohoda, A. Brieland-Shoultz, E.S. Polsen, N.T. Dee, V.S. Veerasamy, A.J. Hart, "Direct fabrication of graphene on $SiO_2$ via thin film stress engineering. *Scientific Reports*, vol. 4, pp. 5049, 2014.

# Asymmetric Growth of Bilayer Graphene on Copper Enclosures Using Low-pressure Chemical Vapor Deposition

W. Fang, A.L. Hsu, Y. Song, A.G. Birdwell (US Army Research Laboratory), M. Dubey (US Army Research Laboratory),
T. Palacios, M.S. Dresselhaus, J. Kong

In this work, we investigated the growth mechanisms of bilayer graphene on the outside surface of Cu enclosures at low pressures. We observed that the asymmetric growth environment of a Cu enclosure can yield a much higher (up to 100%) bilayer coverage on the outside surface than the bilayer growth on a flat Cu foil, where both sides are exposed to the same growth environment.

By inspecting the evolution of the two surfaces of the Cu enclosure during the low-pressure chemical vapor deposition synthesis, we have gained a better understanding of the bilayer growth mechanism on the outside surface of the enclosure. We conclude that the two surfaces are coupled by carbon diffusion through the Cu foil. By identifying the pathways for methane gases and active carbon, we found that carbon diffusing through the Cu foil allows for a continual growth of bilayers from underneath the outside monolayer graphene. Based on the monolayer graphene growth on the inside surface and the inter-copper carbon diffusion process, we derived a growth model for the bilayer graphene on the outside that agrees well with the experimental findings. Finally, we verified our model by measuring the thickness dependence of the Cu foil on the delivery rate of carbon. Moreover, utilizing inter-catalyst diffusion pathways may serve as a more general method for synthesis of other layer-by-layer hybrid structures, such as graphene on h-BN or isotopic bilayer systems. The improved understanding of the synthesis of bilayer graphene on Cu catalysts will lead to the better control of bilayer graphene growth for future bilayer graphene-based devices and potentially other bilayer nano-materials.

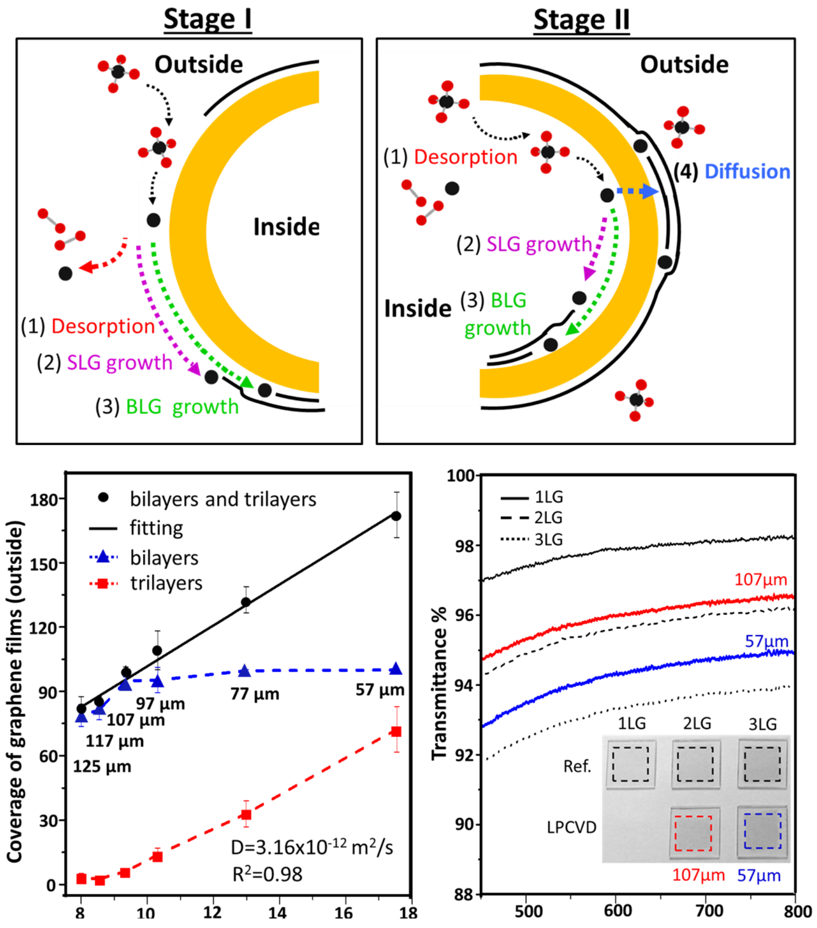

◀ Figure 1:| Growth mechanism of bilayer graphene. (a) Growth mechanism for bilayer graphene on outside surface in stage I, when monolayer graphene is incomplete. (b) Growth mechanism for bilayer graphene in stage II, after completion of monolayer graphene at outside surface. (c) Coverage of bilayers (dotted blue), trilayers (dotted red) and summation of both bilayers and trilayers (dotted black) as a function of thickness of Cu foil. Solid black line shows linear fitting of carbon content. (d) Transmittance of layer-by-layer transferred graphene films (black) and directly grown graphene films on Cu enclosures with thickness of 107 µm (red) and 57 µm (blue), respectively. Inset shows photograph of corresponding graphene films on borosilicate. Layer-by-layer transferred graphene was used as reference.

## FURTHER READING

- W. Fang, A. L. Hsu, R. Caudillo, Y. Song, A. G. Birdwell, E. Zakar, M. Kalbac, M.. Dubey, T. Palacios, M. S. Dresselhaus, P. T. Araujo, J. Kong, "Rapid Identification of Stacking Orientation in Isotopically Labeled Chemical-Vapor Grown Bilayer Graphene by Raman Spectroscopy," *Nano Lett.* 2013.

# Correlation of Shape Changes of Grain Surfaces and Reversible Compressive Stress Evolution in Polycrystalline Films

H.Z. Yu, C.V. Thompson

Sponsorship: National Science Foundation

Polycrystalline thin films typically grow by the Volmer-Weber mechanism, in which the atoms condense on the substrate and diffuse to form nuclei, and the nuclei then grow into 3D islands. Further deposition leads to impingement and coalescence of the 3D islands and formation of grain boundaries, resulting in a tensile stress in the film. Under conditions of high atomic mobility, the post-coalescence stress evolves to a compressive state during film thickening, but the stress evolves toward the tensile direction when growth is interrupted. Remarkably, for short interruptions, when growth is resumed, the stress evolves back to the pre-interruption level. One example of such behavior is shown for Ni films deposited at 473K in Figure 1. Understanding the mechanisms for this complex stress evolution has been the focus of much recent research. Most recently, the stress evolution during a growth interruption has been shown to involve multiple kinetic processes, which can be interpreted as a fast reversible process and a slow irreversible process. The slow process was shown to correspond to a process occurring in the bulk of the film and can be attributed mostly to grain growth after deposition. The underlying mechanism for the fast process is still not clear.

Here we report correlated characterization of stress evolution with evolution of the surface structure of polycrystalline nickel films based on atomic force microscopy (AFM) measurements. Figure 2(a) shows the distribution of inclination angles on Ni film surfaces after 0-, 15-, and 60-min growth interruptions. As the interruption time is increased, the distribution curve moves toward the higher inclination angles, i.e., the surface becomes rougher, with regions of higher surface steepness. Also shown in Figure 2(a) is the distribution of inclination angles after a 60-min interruption, followed by a continued growth of 40 nm and a 15-min interruption (in red). Clearly, the subsequent 40-nm deposition and 15-min interruption led to a leftward shift of the curve back to low inclination angles. Overall, the rightward shift of the curve to high inclination angles going from a 15-min to a 60-min interruption and the leftward shift of the curve back to low inclination angles after the subsequent 40-nm deposition and 15-min interruption demonstrate that the change of the surface structure, as characterized using ex situ AFM, is reversible. Representative cross-sectional transmission electron microscopy (TEM) images are shown in Figures 2 (b) and (c) for Ni films after 0-min and 60-min growth interruptions. Deep grooves were observed at the grain boundaries in the latter film but not in the former film, in which the grooves were generally shallow and flat. The AFM and TEM results suggest that the fast reversible stress evolution is associated with reversible changes in the shapes of the surfaces of individual grains (i.e., grooving and flatting) that occur during growth interruptions and upon growth resumption.

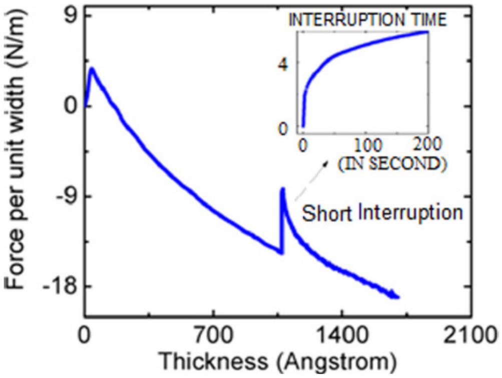

▲ Figure 1: Stress evolution during deposition of a polycrystalline Ni film, including a reversible stress change during an interruption of growth.

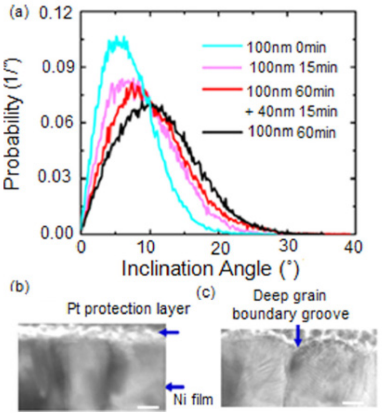

▲ Figure 2: (a) Inclination angle distribution on the surface of Ni films at different times after growth was interrupted. Cross-sectional TEM images after (b) 0-min and (c) 60-min interruptions.

## FURTHER READING

- E. Chason et al., "Origin of compressive residual stress in polycrystalline thin films," *Physical Review Letters*, vol. 88, no. 15, p. 156103, 2002.
- H. Z. Yu, J. S. Leib, S. T. Boles, and C. V. Thompson, "Fast and slow stress evolution mechanisms during interruptions of Volmer-Weber growth," *Journal of Applied Physics*, vol. 115, p. 043521, 2014.
- H. Z. Yu and C. V. Thompson, "Correlation of shape changes of grain surfaces and reversible stress evolution during interruptions of polycrystalline film growth," *Applied Physics Letters*, vol. 104, p. 141913, 2014.

# Quantitative Analysis and Modeling of Templated Solid-state Dewetting of Thin Single-crystal Ni Films

G.H. Kim, R. V. Zucker, W.C. Carter, W. Bao, D.J. Srolovitz, C.V. Thompson
Sponsorship: SMART, National Science Foundation

Thin films are generally metastable in the as-deposited state and will dewet (agglomerate) when heated. Nanometer scale films (<100 nm thick) can dewet at temperatures well below the melting temperature of the film, and dewetting occurs while the film remains solid. This phenomenon can limit the use of very thin films in microsystems, but it can also be used to controllably produce complex structures. Dewetting occurs through retraction of the edges of naturally forming holes or at patterned edges of films. In single-crystal films, anisotropy in surface energy and diffusivity drives the dewetting process to result in regular patterns that relate to the crystal symmetry. We are investigating use of anisotropic dewetting as a self-assembly method to generate complex, small, predetermined patterns. A quantitative understanding of dewetting mechanisms is critical for design of self-assembled structures made through dewetting. We measured the rates of anisotropic edge retraction by solid-state dewetting in kinetically stable edge orientations. These measurements can also be used to estimate the edge retraction rates in a general crystallographic orientation. Additionally, we developed an analytical model for solid-state dewetting via surface diffusion for fully faceted materials to test our understanding of dewetting mechanisms (see Figure 1). This two-dimensional model provides excellent agreement with experimental edge retraction rates for kinetically stable edges. We also developed a three-dimensional phase-field model for dewetting of materials with isotropic surface energies. A three-dimensional model for dewetting of materials with anisotropic surface energies is under development.

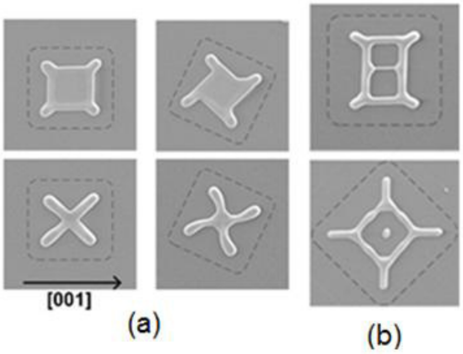

▲Figure 1: (a) Partially dewetted patches patterned from a (100) film into squares with different in-plane orientations; top is an earlier time than bottom. (b) Dewetting patterns of larger squares.

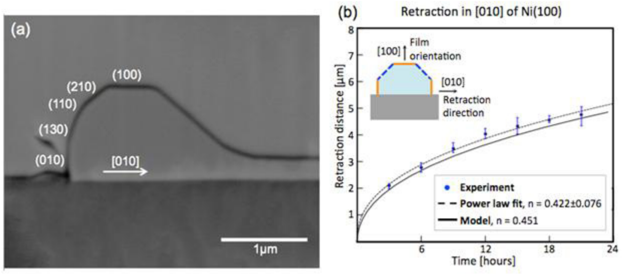

▲Figure 2: (a) Cross-sectional SEM image of a [010] edge in a (100) film. (b) Corresponding experimental and theoretical retraction distance vs. time.

---

## FURTHER READING

- J. P. Ye and C. V. Thompson, "Templated solid state dewetting to controllably produce complex patterns," *Advanced Materials,* vol. 23, pp. 1567-1571, 2011.
- G. H. Kim, R. V. Zucker, W. C. Carter, and C. V. Thompson, "Quantitative analysis of anisotropic edge retraction by solid-state dewetting of thin single crystal films," *Journal of Applied Physics,* vol. 113, 043512, 2013.
- R. V. Zucker, G. H. Kim, W. C. Carter, and C. V. Thompson, "A model for solid state dewetting of a fully faceted thin film," *C. R. Phys.*, vol. 14, pp. 564-577, 2013.

# Understanding Electronic, Optical and Thermal Properties of Transition Metal Chalcogenides

C. Ataca, R. Raghunathan, J.C. Grossman

The fundamental properties of a material depend on its atomic structure, nature of bonding, and elemental/chemical composition. Confinement of electrons in 2-dimensional planar structures leads to the realization of several intriguing properties that are not seen in the bulk 3-dimensional counterparts. In this work, we explore the properties of single- and few- layer MX (M: transition metal, X: chalcogen atom) both theoretically and experimentally. Using state-of-the-art density functional theory (DFT), we carried out a stability analysis through phonon, electronic, magnetic, and elastic structure calculations where M=Cu, Ag, and Au and X=S, Se, and Te. The stacking of transition metal chalcogenide (TMC) monolayers is of the type MX-M2X2 instead of the usual X-M-X stacking found in TMCs. The differences in geometric structure result in many different stable monolayer forms with different electronic and magnetic properties. Depending on the number of layers, MX structures can be found in 2-, 3-, 4- and 6-MX layer stable configurations. Experiments confirm these dimensionality effects predicted by DFT, such as energy band structures and Raman active modes,. Various different monolayers of MX possess a number of properties that make them highly promising materials for future nanoscale applications.

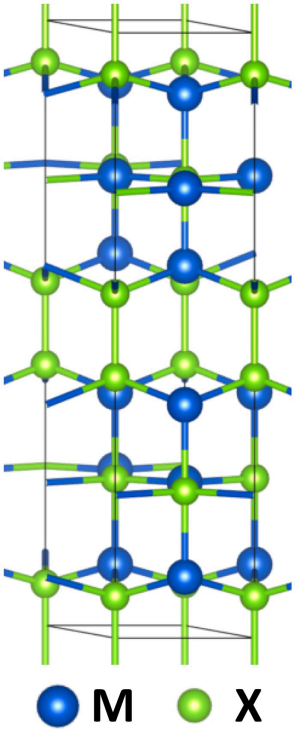

◀ Figure 1: Bulk geometric structure of MX compounds. M: Transition metal; X: Chalcogen atom.